NANO LETTERS

pubs.acs.org/NanoLett Letter

Nonreciprocal-Like Chiral Second-Harmonic Generation in a Chiral 3R-MoS_2 Metasurface

Yi Zhu,[#] Yu-Heng Hou,[#] Qing Cai, Li-Jiong Chen, Ruwen Peng,* and Mu Wang*

Cite This: https://doi.org/10.1021/acs.nanolett.6c00536 Read Online

ACCESS | Metrics & More | Article Recommendations | Supporting Information

ABSTRACT: Breaking reciprocity in nonlinear optics offers a unique approach for directional control of information processing. Here, we report for the first time a chiral 3R-MoS_2 metasurface that enables nonreciprocal-like chiral second-harmonic generation (SHG) via nonreciprocal circularly polarized (CP) absorption. The metasurface supports Mie resonances due to the high refractive index of 3R-MoS_2. With CP incidence around the resonant wavelength on the top surface, right-handed circular polarization (σ_+) absorption is significantly stronger than left-handed circular polarization (σ_-), leading to chiral SHG with a circular dichroism (SHG-CD) of 62%. Reversing the incidence direction inverts the absorption contrast, yielding an SHG-CD of −71%. Physically, such an optical response originates from both the intrinsic C_{3v} symmetry of 3R-MoS_2 and the structural chirality of the metasurface. Leveraging this property, we further demonstrate four optical logic operations, AND, OR, A ANDNOT B, and A ORNOT B, revealing the metasurface as a multifunctional, polarization-dependent platform for optical logic.

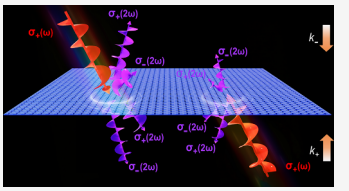

KEYWORDS: *nonreciprocal second-harmonic generation, chiral metasurfaces, nonlinear emission of transition-metal dichalcogenides, nonlinear metasurfaces, transition-metal dichalcogenide metasurfaces*

Optical nonreciprocity enables asymmetric light transmission when its sources and detectors are exchanged.[1−5] Although most materials are reciprocal and thus support bidirectional propagation,[6] many photonic components rely on unidirectional transport,[7] which is specifically useful in optical information processing. Generally, nonreciprocity can be achieved through three mechanisms:[8] magneto-optical media with asymmetric electromagnetic tensors,[9−12] time-varying refractive-index modulation that shifts the frequency and momentum of light,[2,13,14] and nonlinear interactions in geometrical or compositional asymmetric structures[15,16] that produce direction-dependent local fields.[8,17] In optical media with absorption, asymmetric electromagnetic tensors can give rise to nonreciprocal absorption.[18−20] Recent studies have shown that some chiral organic thin films[21,22] exhibit nonreciprocal circularly polarized (CP) absorption,[23,24] in which the handedness of the preferentially transmitted CP component is nearly inverted when light enters from the opposite side of the film.[25,26] In this Letter, we explore nonreciprocal CP absorption in nanostructured transition-metal dichalcogenides and demonstrate its effect on nonlinear emission.

Monolayer or rhombohedral (3R) transition-metal dichalcogenides (TMDs) intrinsically lack inversion symmetry, which is an essential property for nonlinear photonics and optoelectronic applications.[27−30] Their significant second-order susceptibility $|\chi^2|$ enables efficient second-harmonic generation (SHG).[31,32] Normally, the strategies for modulating the SHG response in TMDs fall into two categories.[33] One approach is to engineer the symmetry of the material through van der Waals stacking,[34−37] defect engineering,[38] strain fields,[39] or electric-magnetic control.[40] The other approach modifies the electromagnetic environment, thereby enhancing resonant light−matter interactions and nonlinear response. Metasurfaces provide an efficient platform for locally tailoring the electromagnetic field, including its amplitude, polarization, and phase at the subwavelength scale.[41−47] Accordingly, integrating TMDs with metasurfaces[48−53] can significantly boost SHG via plasmonic or Mie resonances. Besides, the high refractive index of TMDs ($n > 4$)[54] enables their incorporation directly into dielectric nanostructures, leveraging Mie modes[55−57] or quasi-bound states in the continuum[32,58−61] to tailor nonlinear emission. In previous studies, the rule for introducing nanostructures has primarily been to enhance the fundamental-frequency absorption of TMDs, thereby boosting their nonlinear optical responses. Now we consider that chiral structures may exhibit nonreciprocal CP absorption, which may further induce a nonreciprocal-like chiral nonlinear emission and also enrich the scope of chiral optics.[62−65] To the best of our knowledge, such an effect has not yet been reported so far.

In this Letter, we demonstrate a chiral 3R-MoS_2 metasurface that exhibits nonreciprocal CP absorption, leading to strongly nonreciprocal-like chiral second-harmonic generation (SHG).

Received: February 1, 2026
Revised: March 30, 2026
Accepted: April 1, 2026

https://doi.org/10.1021/acs.nanolett.6c00536
Nano Lett. XXXX, XXX, XXX−XXX

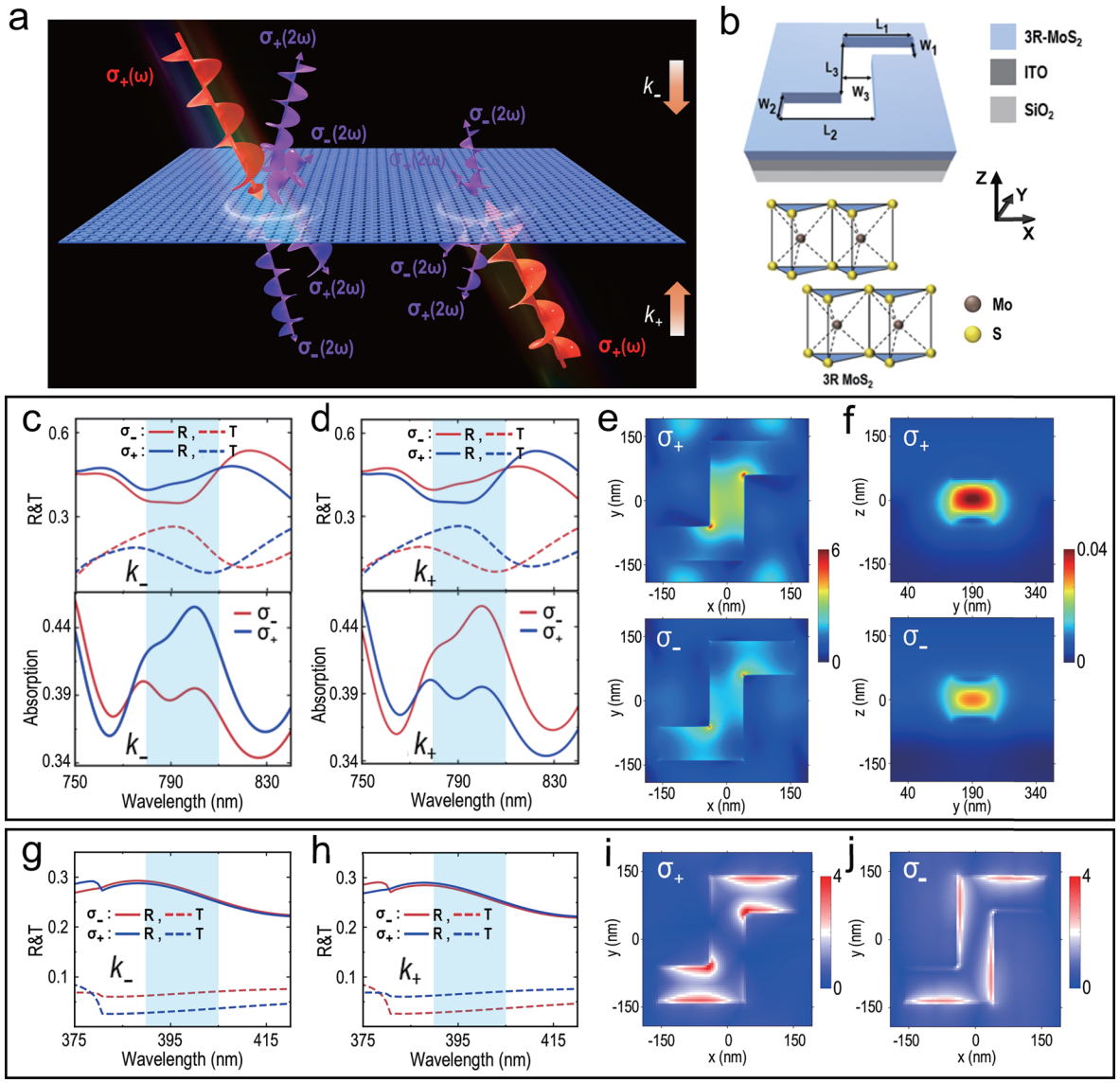

Figure 1. (a) Schematic of the nonreciprocal chiroptical effect of the 3R-MoS_2 metasurface. Here only σ_+ excitation is shown. (b) The upper panel shows the unit cell of the 3R-MoS_2 metasurface on the ITO-deposited SiO_2 substrate, which has the geometrical parameters $L_1 = L_2 = L_3 = 200$ nm, $W_1 = W_2 = W_3 = 80$ nm, and the periodicity $P_x = P_y = 380$ nm. The thickness of the 3R-MoS_2 metasurface is 110 nm. The lower panel shows the schematic of the atomic structure of 3R-MoS_2. (c) and (d) The simulated transmission, reflection and absorption spectra of the 3R-MoS_2 metasurface under CP (σ_+ or σ_-) light illumination along the k_ or k_+ direction. The blue-gray shaded region highlights the excitation wavelength range from 780 to 810 nm. (e) and (f) are, respectively, the simulated electric field distribution and magnetic field across the unit cell under σ_+ and σ_- illumination ($\lambda = 800$ nm) along the k_ direction. (g) and (h) The simulated transmission and reflection spectra of the 3R-MoS_2 metasurface under CP (σ_+ or σ_-) light illumination along the k_ or k_+ direction around the wavelength of 400 nm. The blue-gray shaded region highlights the excitation ranging from 390 to 405 nm. (i) and (j) Simulated LDOS of the 3R-MoS_2 metasurface with dipole excitation ($\lambda = 400$ nm) of σ_+ and σ_-, respectively. Both are viewed in the k_ direction.

For the normal incident excitation from the top side, the metasurface absorbs right-handed circular polarization (σ_+) light more strongly than left-handed circular polarization (σ_-) light, resulting in chiral SHG with an SHG circular dichroism (SHG-CD) of 62%. When the excitation direction is reversed, the absorption contrast inverts accordingly; i.e., σ_+ absorption is suppressed with respect to σ_-, yielding chiral SHG with SHG-CD around −71%. Across the 780−810 nm excitation wavelength range, the average absolute value of SHG-CD reaches about 68%, confirming the robust broadband feature. Leveraging this direction- and polarization-sensitive SHG response, we further show that the metasurface can implement optical logic operations: linearly polarized beams enable AND and OR functions through threshold selection, while CP input beams realize A ANDNOT B and A ORNOT B functions.

We first present the design principle and then apply finite-difference time-domain (FDTD) simulations to investigate the nonreciprocal chiroptical response of a 3R-MoS_2 metasurface. Figure 1a illustrates a chiral 3R-MoS_2 metasurface consisting of a Z-shaped nanohole array supporting Mie resonances due to the high refractive index of 3R-MoS_2. We define the k_ direction as the normal incidence from the top to the bottom of the metasurface, with k_+ denoting the opposite direction. The Mie resonance modes at the fundamental frequency depend on chirality pronouncedly, and their responses differ for k_ and k_+ excitation, resulting in nonreciprocal CP

https://doi.org/10.1021/acs.nanolett.6c00536
Nano Lett. XXXX, XXX, XXX−XXX

absorption and consequently nonreciprocal-like chiral SHG. For CP illumination from the k_ direction, absorption of σ_+ light significantly exceeds that of σ_- light due to the chirality of the metasurface, resulting in stronger SHG under σ_+ excitation. Additionally, owing to the intrinsic C_{3v} symmetry of 3R-MoS_2, the SHG exhibits pronounced polarization selectivity: under σ_+ (σ_-) excitation from the k_ direction, the SHG propagating along k_+ direction is dominated by the σ_+ (σ_-) component, while the opposite SHG propagation direction favors the complementary polarization. These features collectively reveal the chiral nature of the SHG. In contrast, for CP illumination from k_+, σ_+ absorption is suppressed relative to σ_- absorption, leading to weaker SHG under σ_+ excitation. The distinct chiral SHG responses for opposite excitation directions confirm the emergence of nonreciprocal-like chiral SHG in the 3R-MoS_2 metasurface.

In such a 3R-MoS_2 metasurface, the resonant wavelength is designed at 800 nm by selecting $L_1 = L_2 = L_3 = 200$ nm, $W_1 = W_2 = W_3 = 80$ nm, and the periodicity $P_x = P_y = 380$ nm (Figure 1b). Figure 1c,d presents the calculated reflection, transmission, and absorption spectra of the 3R-MoS_2 metasurface under illumination from the k_ and k_+ directions, respectively. It follows that when light illuminates the metasurface along k_ direction with wavelength 800 nm, σ_+ light has a higher reflectance (R) and a lower transmittance (T) than σ_- light, as shown in the upper panel of Figure 1c. The optical absorption (A) is defined as $A = 1 - R - T$, as illustrated in the lower panel of Figure 1c. One may find that the metasurface exhibits higher absorption in σ_+ excitation than that in σ_- excitation around resonant wavelength (800 nm). In contrast, when the light excites the metasurface along k_+ direction, σ_- possesses a higher reflectance than σ_+, while σ_+ exhibits greater transmittance than σ_-, as demonstrated in the upper panel of Figure 1d. Meanwhile, the metasurface exhibits a lower absorption for σ_+ excitation than σ_- excitation around resonant wavelength (800 nm), as indicated in the lower panel of Figure 1d.

To explore the physical mechanism of the difference in absorption, we simulate the electric and magnetic field distributions at the wavelength of 800 nm in the $x-y$ plane and $y-z$ plane for both σ_+ and σ_- excitations along the k_ direction, as illustrated in Figures 1e and 1f, respectively. This confirms that it is a Mie resonance mode,[66,67] where both the electric and magnetic field intensities are higher in σ_+ excitation, resulting in differences in the CP-dependent absorption spectra. The resonant modes of the fabricated 3R-MoS_2 metasurfaces have also been investigated (more details in Supporting Information S1).

The SHG response from the 3R-MoS_2 metasurface depends on the handedness of the incident CP light and the excitation direction. When the incidence is in the k_ direction, the intensity of SHG is higher for σ_+ excitation than σ_- excitation, independent of the propagation direction of the SHG signals. When the excitation propagates in k_+, the SHG intensity is higher for σ_- excitation than that for σ_+ excitation, which is also independent of the propagation direction of the SHG signals. Furthermore, we can obtain the polarization of the SHG signals by analyzing the second-order nonlinear dipole response. It is known that 3R-MoS_2 possesses C_{3v} symmetry.[68] The intrinsic nonlinear susceptibility tensor $\chi^{(2)}$ of 3R-MoS_2 has four nonzero, identical terms,[69,70] $\chi^{(2)} = \chi_{xxx} = -\chi_{xyy} = -\chi_{yyx} = -\chi_{yxy} = \chi$, where the x-direction is defined as the armchair direction. It follows that the second-order nonlinear dipole response[69] can be written as $P_x = \varepsilon_0\chi(E_x^2 - E_y^2)$, and $P_y = -2\varepsilon_0\chi E_x E_y$. We can transform the $x-y$ linear polarization basis into the circular polarization basis. In the circular polarization basis, $P_- = \sqrt{2}\,\varepsilon_0\chi E_+^2$ and $P_+ = \sqrt{2}\,\varepsilon_0\chi E_-^2$. Here

$$P = (P_-, P_+)^T = (P_x - iP_y, P_x + iP_y)^T/\sqrt{2},$$
$$E = (E_-, E_+)^T = (E_x - iE_y, E_x + iE_y)^T/\sqrt{2}$$

It is noteworthy that the fundamental wave is incident in the k_ direction, and the circular polarization states of the SHG signals propagating along the reflection and transmission directions are not identical. The SHG electric fields in the reflection and transmission directions can be expressed as[71]

$$P^{2\omega}_{k_+,\pm} \propto \sqrt{2}\chi(E^{\omega}_{\pm})^2 \quad (1)$$

$$P^{2\omega}_{k_-,\pm} \propto \sqrt{2}\chi(E^{\omega}_{\mp})^2 \quad (2)$$

This means that when a specific CP light is incident along the k_ or k_+ direction, the SHG signals possess distinct polarization characteristics in the reflection and transmission directions. For the reflected SHG, the copolarized component is stronger than the cross-polarized one. For the transmitted SHG, the cross-polarized component is stronger than the copolarized one.

Based on the C_{3v} symmetry of 3R-MoS_2, the circular polarization components of the SHG can be preliminarily determined. However, the SHG emission is also influenced by the chiral Purcell effect[72−74] in the 3R-MoS_2 metasurface. We first simulate transmission and reflection spectra of the 3R-MoS_2 metasurface under CP light illumination around SHG frequency (to see Figure 1g and 1h around the wavelength of 400 nm). Then by defining ρ_+ (or ρ_-) as the local density of states (LDOS) on the metasurface with σ_+ (or σ_-) dipole excitation and ρ_0 as the LDOS in the vacuum, we can calculate the normalized circularly polarized LDOS,[72,75] i.e., ρ_+/ρ_0 (or ρ_-/ρ_0). Figure 1i and 1j shows the simulated LDOS of the 3R-MoS_2 metasurface with σ_+ and σ_- dipole excitation at the wavelength of 400 nm, respectively, as viewed along the k_ direction. When viewed along the k_+ direction, the LDOS has the same distribution but exchanged CP excitation type. The LDOS is stronger under σ_+ dipole excitation. This suggests that the 3R-MoS_2 metasurface promote a higher spontaneous emission rate for σ_+ dipoles, thereby yielding a higher Purcell factor for σ_+ SHG emission.

In experiments, the chiral 3R-MoS_2 metasurface is fabricated as follows. We first place a mechanically exfoliated 3R-MoS_2 layer (110 nm in thickness) onto an ITO/SiO_2 substrate via dry transfer. Then, the metasurface structures are fabricated on the 3R-MoS_2 film by a dual-beam focused ion beam (FIB) milling system. An optical microscope image of the 3R-MoS_2 metasurface is shown in the upper panel of Figure 2a, with the sample size as 9.5 μm. The scanning electron micrograph of the 3R-MoS_2 metasurface is illustrated in the lower panel of Figure 2a, with magnified structural details illustrated in the inset. With the incident CP light illuminating the 3R-MoS_2 metasurface along the k_ direction, the experimentally measured reflection and transmission spectra of the MoS_2 metasurface are illustrated in the upper panel of Figure 2b. The absorption spectra are illustrated in the lower panel of Figure 2b. The absorption of the 3R-MoS_2 metasurface in σ_+ light excitation is higher than that with σ_- light excitation at the wavelength of 800 nm. When the 3R-MoS_2 metasurface is illuminated in the k_+ direction, the measured reflection and

https://doi.org/10.1021/acs.nanolett.6c00536
Nano Lett. XXXX, XXX, XXX−XXX

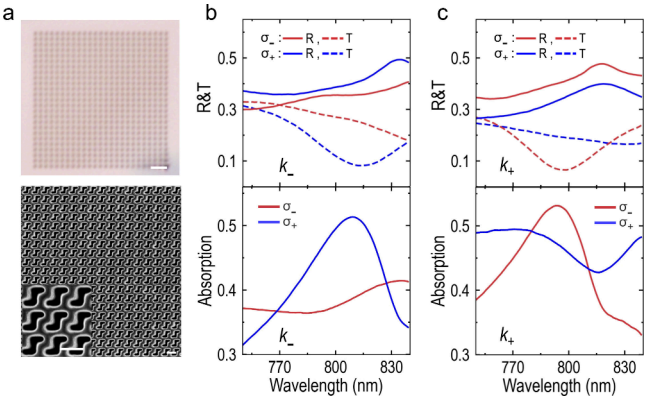

Figure 2. (a) Optical microscope image (upper panel) of the 3R-MoS_2 metasurface, where the scale bar is 1 μm. The scanning electron micrographs (lower panel) of the 3R-MoS_2 metasurface, where the scale bar is 380 nm. The inset in the lower panel shows a magnified view of the 3R-MoS_2 metasurface, where the scale bar stands for 380 nm. (b) and (c) The measured reflection, transmission, and absorption spectra of the 3R-MoS_2 metasurface under CP (σ_+ or σ_-) light illumination along the k_ and k_+ direction, respectively.

transmission spectra for CP light illumination are shown in the upper panel of Figure 2c. The absorption spectra are presented in the lower panel of Figure 2c. The absorption of the 3R-MoS_2 metasurface in σ_+ excitation is lower than that in σ_- excitation at a wavelength of 800 nm. These observations are reasonably consistent with the simulations shown in Figure 1c and 1d, although there exist some deviations originating mainly from fabrication imperfections, systematic errors of the experimental setup, and the substrate effect. Specifically, all the numerical simulations in Figure 1 are for the 3R-MoS_2 metasurface without any substrate, whereas in the experiments, the ITO/SiO_2 substrate clearly enhances the structural asymmetry along the z direction, which may alter the transmittance and reflectance of σ_- and σ_+ in the k_ and k_+ directions. For circularly polarized incidence, the absorption difference between σ_- and σ_+ becomes larger in the k_ direction and smaller in the k_+ direction.

Considering that the 3R-MoS_2 metasurface possesses different absorption at illumination of CP light in the k_ and k_+ directions, we now focus on nonreciprocal-like chiral SHG by measuring the SHG spectra. Figures 3a and 3b illustrate the optical setup for measuring the SHG signals of the 3R-MoS_2 metasurface. A femtosecond pulsed laser (800 nm) is applied to excite the sample. The beam passes through a polarizer and a quarter-wave plate in sequence and then excites the metasurface in k_ or k_+ directions, respectively. The SHG propagating in the k_+ direction is collected by a spectrometer after passing through a 405 nm short-pass filter, a quarter-wave plate, and a linear polarizer in sequence. Figure 3c shows the SHG intensity collected in k_+ direction by exciting the 3R-MoS_2 metasurface in k_ direction, where a quadratic relationship with the pump laser power is presented in the inset of Figure 3c. Then, we measure the CP-resolved SHG spectra, as illustrated in the upper panel of Figure 3d, where $\sigma_+/\sigma_\pm$ represents the $\sigma_\pm$ resolved SHG spectra excited by the σ_+ incidence, and $\sigma_-/\sigma_\pm$ stands for the $\sigma_\pm$ resolved SHG spectra excited by the σ_- incidence. With σ_+ excitation on the metasurface, the σ_+ component of SHG intensity is higher than the σ_- component. With σ_- excitation, the σ_- component of SHG intensity is higher than the σ_+ component instead. The differences of these polarization components originate from both the C_{3v} symmetry of 3R-MoS_2 and the structural chirality of the metasurface. Meanwhile, the sum of the SHG intensities measured in the σ_+/σ_- and the σ_+/σ_+ is greater than the sum of the SHG intensities measured in the σ_-/σ_- and the σ_-/σ_+, suggesting that σ_+ can generate a more vigorous SHG intensity than σ_-. In addition, compared with bare 3R-MoS_2 film (Supporting Information S2), with σ_+ excitation in the k_ direction, the SHG intensity from the metasurface is approximately twice that of the bare film, whereas with σ_- excitation, the SHG intensity of the metasurface is comparable to that of the bare film. This feature mainly originates from the chirality-dependent Mie resonance designed at the fundamental frequency. In principle, the chiral SHG efficiency can be further improved in an optimized chiral metasurface, where both the Mie resonance at the fundamental frequency and the Purcell effect at the frequency of SHG are elaborately designed to enhance the SHG efficiency further.

Furthermore, we measure the SHG spectra under linearly polarized excitation in the k_ direction, as illustrated in the lower panel of Figure 3d, where the x-polarized direction is defined as the x-axis shown in Figure 1b. The x-polarized light yields higher SHG intensity than the y-polarized light. We attribute this effect to the stronger electric field excited in the 3R-MoS_2 metasurface by x-polarized incidence, which enhances absorption of x-polarized light, thereby increasing the SHG intensity (Supporting Information S3). Since the chiral nanostructure can modulate both the polarization of incident light and the polarization of emitted SHG, we further measured the Stokes parameters[76,77] of the emitted SHG with circularly and linearly polarized excitation, as illustrated in Figure 3e. With CP excitation, the emitted SHG is predominantly elliptically polarized, whereas with linear polarized excitation, the SHG remains linearly polarized.

Next, we excite the 3R-MoS_2 metasurface with k_+ excitation and collect the transmitted SHG signal propagating along the same k_+ direction (as shown in Figures 3f-3h). Due to the nonreciprocal CP absorption of 3R-MoS_2 metasurface, the CP-resolved SHG spectra demonstrate a different response, as illustrated in the upper panel of Figure 3g. The sum of the SHG intensity measured in σ_+/σ_- and σ_+/σ_+ configurations is lower than the sum of the SHG intensity measured in σ_-/σ_- and σ_-/σ_+ configurations, suggesting that σ_- incidence can generate a more vigorous SHG intensity than σ_+ incidence. In contrast, for the linearly polarized excitation SHG spectrum, x-polarized incidence generates higher SHG intensity than y-polarized incidence. We also measured the CP-resolved SHG spectra corresponding to the SHG signals propagating in the k_ direction (Supporting Information S4).

Subsequently, our work on the circular dichroism (CD) and linear dichroism (LD) of the SHG from 3R-MoS_2 metasurface is defined as[78,79] $\mathrm{CD} = 2 \times \frac{I_{\sigma+/\sigma-} + I_{\sigma+/\sigma+} - I_{\sigma-/\sigma-} - I_{\sigma-/\sigma+}}{I_{\sigma+/\sigma-} + I_{\sigma+/\sigma+} + I_{\sigma-/\sigma-} + I_{\sigma-/\sigma+}}$, and $\mathrm{LD} = 2 \times \frac{I_x - I_y}{I_x + I_y}$, where $I_{\sigma+/\sigma+}$ represents the σ_+ component of SHG in σ_+ excitation, $I_{\sigma+/\sigma-}$ represents the σ_- component of SHG in σ_+ excitation, $I_{\sigma-/\sigma+}$ represents the σ_+ component of SHG in σ_- excitation, $I_{\sigma-/\sigma-}$ represents the σ_- component of SHG in σ_- excitation; and I_x and I_y denote the SHG intensities in x- and y-polarized excitation, respectively. Along the k_ direction, for CP excitation around 800 nm, the SHG-CD is positive, with a CD of approximately 62% at λ = 400 nm when the SHG is collected in the k_+ direction (see the upper panel of

https://doi.org/10.1021/acs.nanolett.6c00536
Nano Lett. XXXX, XXX, XXX−XXX

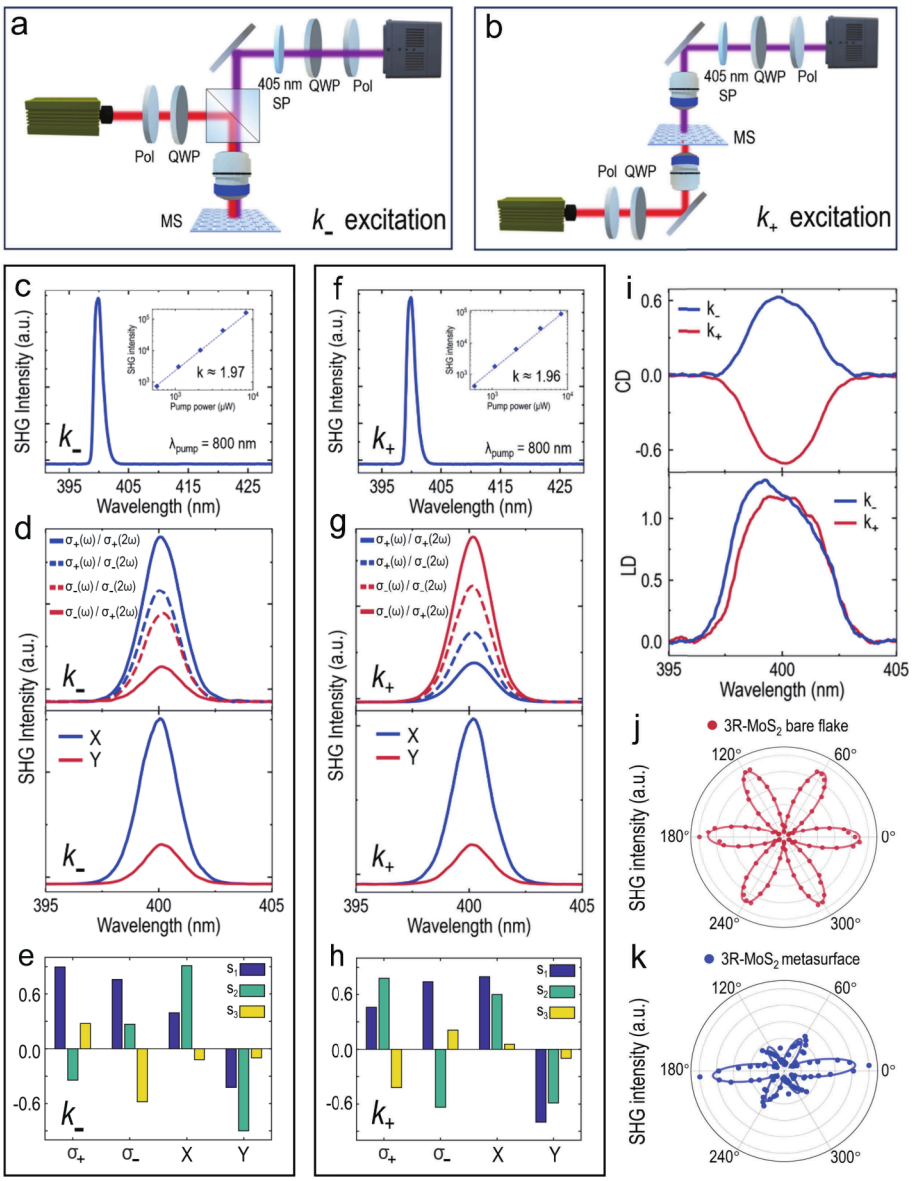

Figure 3. (a) and (b) Schematics of the experimental setup for SHG signal measurements in the k_+ direction under k_- and k_+ excitation, respectively. Here, "Pol" denotes a linear polarizer, "QWP" denotes a quarter-wave plate, "405 nm SP" denotes a 405 nm short-pass filter, and "MS" denotes the metasurface. (c) and (f) The measured SHG spectrum of the 3R-MoS_2 metasurface under k_- or k_+ excitation at the wavelength of 800 nm. The inset shows the power−power curve of the SHG. (d) and (g) The measured CP-resolved SHG spectra (upper panel) and the SHG spectra under linearly polarized excitation (lower panel) of the 3R-MoS_2 metasurface under k_- or k_+ excitation at the wavelength of 800 nm. Here, $\sigma_+(\omega)/\sigma_-(2\omega)$ means the σ_--polarized SHG intensity at the second-harmonic frequency under σ_+-polarized fundamental-frequency excitation. Other cases are similar. (e) and (h) The measured Stokes parameters of the SHG signals under CP and linearly polarized excitations at the wavelength of 800 nm. (i) For k_- and k_+ excitations at the wavelength of 800 nm, the CD and LD spectra of the measured SHG from the 3R-MoS_2 metasurface. (j) and (k) The measured polarization-resolved SHG of a bare 3R-MoS_2 flake and the 3R-MoS_2 metasurface as a function of the rotation angle ϕ of the pump polarization with respect to the x-axis, respectively. Both are under k_- excitation at the wavelength of 800 nm. The dots are the measured data, and the lines are the fittings.

Figure 3i) and a CD of approximately 58% at λ = 400 nm when the SHG is collected in the k_- direction (Supporting Information S4). With linearly polarized excitation, the SHG-LD is positive, with an LD reaching about 119% at λ = 400 nm (see the lower panel of Figure 3i). While along the k_+ direction, for CP excitation at 800 nm, the SHG-CD becomes negative, and the SHG-CD is −71% at λ = 400 nm when the SHG is collected in the k_+ direction (see the upper panel of Figure 3i), and a CD of −61% when the SHG (λ = 400 nm) is collected in the k_- direction (Supporting Information S4). With a linearly polarized excitation, the SHG-LD remains positive, with an LD reaching about 116% at λ = 400 nm (see the lower panel of Figure 3i). When the incident direction of CP is switched from k_- to k_+, the sign of SHG-CD reverses, confirming that the 3R-MoS_2 metasurface exhibits the nonreciprocal-like chiral SHG under CP excitation. Such a feature arises from the nonreciprocal CP absorption at the fundamental frequency, together with the intrinsic C_{3v} symmetry of 3R-MoS_2. Specifically, in the k_- direction, the σ_+ resonance mode is stronger, leading to stronger σ_+ absorption and thus stronger SHG under σ_+ excitation, which yields a positive CD. In the k_+ direction, the σ_- resonance mode is stronger, leading to

https://doi.org/10.1021/acs.nanolett.6c00536
Nano Lett. XXXX, XXX, XXX−XXX

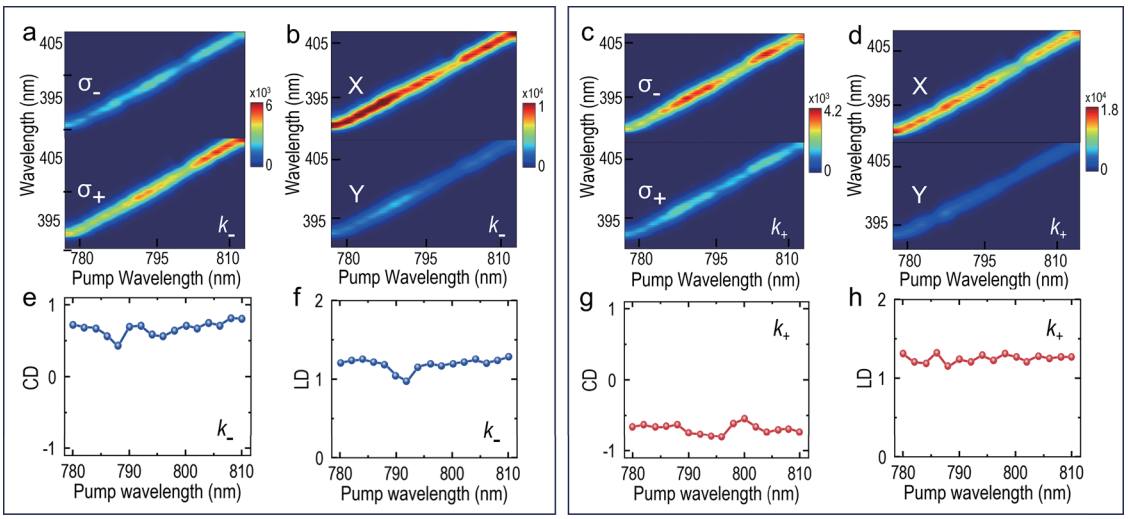

Figure 4. (a) and (c) Measured SHG intensity spectra of the 3R-MoS_2 metasurface excited by CP (σ_+ or σ_-) light along the k_ or k_+ direction at different wavelengths. (b) and (d) The measured SHG intensity spectra of the 3R-MoS_2 metasurface excited by linearly polarized light along the k_ or k_+ direction at different wavelengths. (e) and (g) The CD spectra of the measured SHG from the 3R-MoS_2 metasurface under the CP excitation in the k_ or k_+ direction. (f) and (h) The LD spectra of the measured SHG from the 3R-MoS_2 metasurface under the linearly polarized excitation in the k_ or k_+ direction.

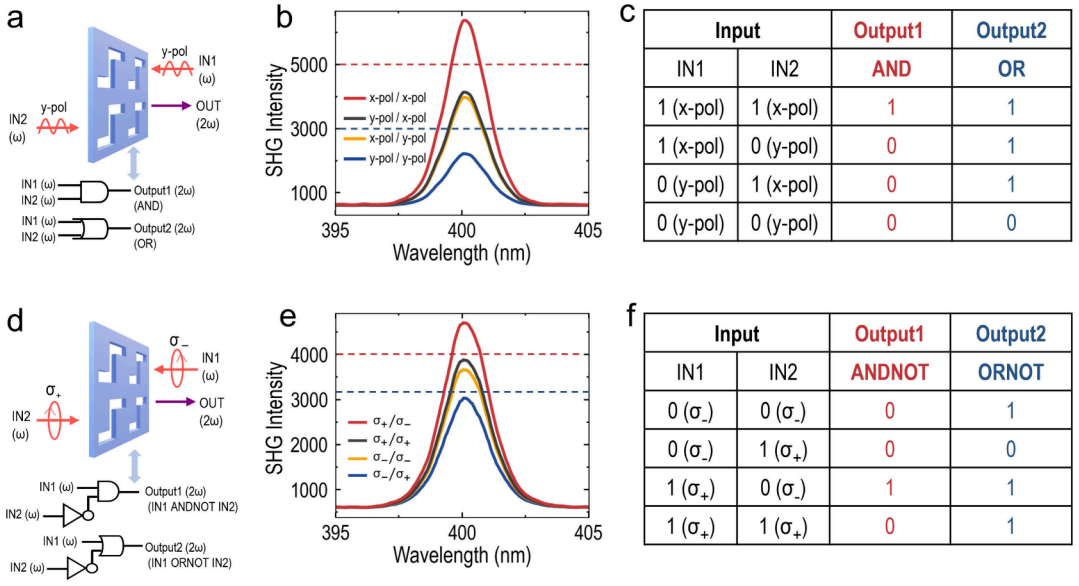

Input		Output1	Output2
IN1	IN2	AND	OR
1 (x-pol)	1 (x-pol)	1	1
1 (x-pol)	0 (y-pol)	0	1
0 (y-pol)	1 (x-pol)	0	1
0 (y-pol)	0 (y-pol)	0	0

Input		Output1	Output2
IN1	IN2	ANDNOT	ORNOT
0 (σ_-)	0 (σ_-)	0	1
0 (σ_-)	1 (σ_+)	0	0
1 (σ_+)	0 (σ_-)	1	1
1 (σ_+)	1 (σ_+)	0	1

Figure 5. (a) Schematic illustration of the AND logic gate and the OR logic gate by using a single metasurface. (b) The experimental output SHG spectra of the 3R-MoS_2 metasurface under the excitation of two linearly polarized lights with λ = 800 nm. Here, *x*-pol/*y*-pol represents the collected output SHG intensity when IN1 is *x*-polarized and IN2 is *y*-polarized. (c) Truth tables for the AND and OR logic gates. (d) Schematic illustration of the IN1 ANDNOT IN2 logic gate and IN1 ORNOT IN2 logic gate. (e) The experimental output SHG spectra of the 3R-MoS_2 metasurface under the excitation of two CP lights with λ = 800 nm. Here, σ_+/σ_- represents the collected output SHG intensity when IN1 is σ_+ and IN2 is σ_-. (f) Truth table of the IN1 ANDNOT IN2 logic gate and IN1 ORNOT IN2 logic gate.

stronger σ_- absorption and stronger SHG under σ_- excitation, resulting in a negative CD. In contrast, the constantly positive SHG-LD indicates that the SHG response remains reciprocal in the linearly polarized excitation.

We also measure polarization-resolved SHG with the incident light propagating in the k_ direction. Figure 3j and 3k shows the measured SHG intensities of a bare 3R-MoS_2 flake (red dots) and the 3R-MoS_2 metasurface (blue dots) as a function of the rotation angle ϕ of the pumping polarization with respect to the *x*-axis, respectively. The data indicate that for the bare 3R-MoS_2 flake, the polarization-resolved SHG intensity possesses a 6-fold symmetric pattern. For the 3R-MoS_2 metasurface, the measured SHG intensities show a clear anisotropy, where the intensity petals a few degrees above zero and a few degrees surpassing 180° have the strongest value, whereas the petals pointing to 120° and 300° are the weakest. These observations suggest that the SHG intensity of the 3R-MoS_2 metasurface exhibits anisotropy depending on the symmetry of the building block of the metasurface.

Achieving broadband nonlinear responses is highly desirable for nonlinear photonic devices. Our designed chiral metasurface, leveraging Mie resonances, is expected to exhibit nonlinear polarization responses across a broad spectral range. We experimentally verify the operating wavelength

https://doi.org/10.1021/acs.nanolett.6c00536
Nano Lett. XXXX, XXX, XXX−XXX

range of the metasurface by sweeping the excitation wavelength and measuring the SHG intensity for σ_+, σ_- and linearly polarized excitations in the k_ and k_+ directions, respectively. For the excitation in the k_ direction, the results are shown in Figures 4a and 4b. The SHG intensity in σ_+ excitation consistently exceeds that in σ_- excitation, and the SHG intensity of *x*-polarized excitation consistently surpasses that of *y*-polarized excitation within the regime of 780−810 nm. For excitation along the k_+ direction, the generated SHG spectra for different polarizations and pump wavelengths are shown in Figure 4c and 4d. The SHG intensity in σ_- excitation consistently exceeds that in σ_+ excitation, and the SHG intensity in *x*-polarized excitation consistently surpasses that of *y*-polarized excitation in the range of 780−810 nm.

As demonstrated in Figure 4e and 4f, the CD and LD spectra of SHG reveal that the 3R-MoS_2 metasurface exhibits positive CD values exceeding 40% and positive LD values consistently exceeding 90% when the incidence is in the k_ direction. The CD and LD spectra of SHG shown in Figures 4g and 4h reveal that the 3R-MoS_2 metasurface exhibits a negative CD with an absolute value consistently exceeding 50%, and a positive LD consistently exceeding 100% when the incidence is in the k_+ direction. For k_ and k_+ excitations, the average absolute SHG-CD is about 68% across the 780−810 nm spectral range. These results confirm that nonreciprocal-like chiral SHG has been achieved with the 3R-MoS_2 metasurface, and both SHG-CD and SHG-LD can be effectively modulated within the range of 780−810 nm.

Based on the SHG responses in the 3R-MoS_2 metasurface, we can construct four polarization-dependent logic gates. Figure 5a illustrates the schematic of AND and OR logic gates, where IN1 represents the input beam in the k_ direction, IN2 represents the input beam in the k_+ direction, and OUT represents the SHG generated by the 3R-MoS_2 metasurface in the k_+ direction. Figure 5b shows the measured SHG spectra for different linearly polarized excitations at 800 nm. When both input beams are x-polarized, the output SHG intensity is the strongest. When IN1 is *x*-polarized, whereas IN2 is *y*-polarized, or in the other way, i.e., IN1 is *y*-polarized and IN2 is *x*-polarized, the output SHG possesses the second strongest intensity. However, once both incidences are *y*-polarized, the output SHG intensity is the weakest. In practice, we can set a threshold in SHG measurements. Once the SHG intensity is below the threshold, the scenario is recorded as "0"; otherwise, it is recorded as 1. In our case, when the threshold is set to 5000 (about 75%), the system behaves as an AND gate; when the threshold is set to 3000 (about 45%), it becomes an OR gate. The truth table for these two logic gates is presented in Figure 5c.

With a CP incidence of 800 nm on the 3R-MoS_2 metasurface, two different logic gates, IN1 ANDNOT IN2 and IN1 ORNOT IN2, can be constructed, as schematically shown in Figure 5d. Figure 5e represents the measured SHG spectra with different CP excitations. When IN1 is in σ_+, and IN2 is in σ_-, the intensity of the output SHG is the strongest. When the two inputs are both in σ_+, or both in σ_-, the output SHG intensity is the second strongest. If IN1 is σ_- while IN2 is σ_+, the output SHG intensity becomes the weakest. Meanwhile, we set a threshold for SHG intensity: below the threshold, the scenario is recorded as "0"; above the threshold, the scenario is recorded as "1". In our experiments, if we set the threshold to 4000 (about 85%), the system works as an IN1 ANDNOT IN2 gate; if we set the threshold to 3200 (about 65%), it works as an IN1 ORNOT IN2 gate instead. The truth table for these two logic gates is presented in Figure 5f. Therefore, we demonstrate here that based on the SHG response, this 3R-MoS_2 metasurface may serve as four types of logic gates: AND, OR, A ANDNOT B, and A ORNOT B, by changing the incident polarization and turning the threshold values.

It is interesting to note that the performance of the polarization-dependent photonic logic gates could be further improved by resolving the SHG helicity, which may significantly enhance the on/off ratio. In addition, since the metasurface can modulate the polarization of emitted SHG, the intensity contrast between different logical states can be modified by introducing additional polarization analyzers. These approaches can advance the applications of photonic logic gates (Supporting Information S5).

In summary, we have demonstrated nonreciprocal-like chiral SHG in a chiral 3R-MoS_2 metasurface. This effect arises from nonreciprocal CP absorption, leading to a direction-dependent nonlinear optical response. Under resonant CP excitation in the k_ direction, the SHG-CD reaches 62%, whereas excitation in the k_+ direction yields an SHG-CD of approximately −71%. Across the 780−810 nm spectral range, the average absolute SHG-CD remains at ∼68%, indicating a robust broadband response. The observed nonreciprocal-like chiral SHG arises from both the structural chirality of the metasurface and the intrinsic C_{3v} symmetry of 3R-MoS_2. Moreover, the 3R-MoS_2 metasurface enables four types of photonic logic operations via the SHG responses: AND/OR gates under linearly polarized excitation, and A ANDNOT B or A ORNOT B gates under CP excitation. These results establish 3R-MoS_2 metasurfaces as a compact and multifunctional platform for integrated nonlinear photonics and photonic logic, enabled by the strong intrinsic nonlinearities and high refractive index of rhombohedral transition-metal dichalcogenides.

SIMULATION

All simulations are carried out using the FDTD method. In the simulation, periodic boundary conditions in the *x*- and *y*-directions and perfectly matched layer (PML) boundary conditions in the *z*-direction are applied. Plane-wave sources with wavelengths in the range 375−840 nm are placed 1 μm from the structure. In the main text, we assume MoS_2 to be isotropic, while in Supporting Information S6, we further consider the anisotropy of MoS_2.

SAMPLE PREPARATION

The 3R-MoS_2 film with a thickness of 110 nm is transferred onto the ITO/SiO_2 substrate using a dry transfer method. The metasurface is fabricated by etching the 3R-MoS_2 film using the dual-beam FIB system (Helios, Nanolab 600i).

MICROSCOPY

The 3R-MoS_2 metasurface is observed with an optical microscope (Nikon, ECLIPSE 80i). Scanning electron micrographs of the 3R-MoS_2 metasurface are obtained with a field-emission scanning electron microscope (Zeiss, ULTRA55).

POLARIZATION-RESOLVED SHG MEASUREMENTS

Polarization-resolved SHG data are observed on a confocal micro-Raman system (Princeton Instruments, Trenton, NJ). The excitation pulses come from a Ti:sapphire mode-locked

https://doi.org/10.1021/acs.nanolett.6c00536
Nano Lett. XXXX, XXX, XXX−XXX

laser with a pulse repetition rate of 80 MHz and, particularly, is centered at a wavelength of 800 nm.

■ ASSOCIATED CONTENT

Supporting Information

The Supporting Information is available free of charge at https://pubs.acs.org/doi/10.1021/acs.nanolett.6c00536.

(i) Scattering cross sections of the 3R-MoS_2 metasurface; (ii) the SHG intensity comparison between the chiral 3R-MoS_2 metasurface and a bare film; (iii) the simulated transmission, reflection, and absorption spectra, as well as the electric field and magnetic field distributions of the 3R-MoS_2 metasurface under linearly polarized excitation; (iv) measuring the CP-resolved SHG of the chiral 3R-MoS_2 metasurface propagating in the k_ direction; (v) the CP-resolved SHG logic gates under CP excitations; and (vi) the simulated transmission, reflection, and absorption spectra of the 3R-MoS_2 metasurface under CP excitation if considering the anisotropy of MoS_2 (PDF)

■ AUTHOR INFORMATION

Corresponding Authors

Ruwen Peng − *National Laboratory of Solid State Microstructures, School of Physics, Collaborative Innovation Center of Advanced Microstructures, and Jiangsu Physical Science Research Center, Nanjing University, Nanjing 210093, China;* orcid.org/0000-0003-0424-2771; Email: rwpeng@nju.edu.cn

Mu Wang − *National Laboratory of Solid State Microstructures, School of Physics, Collaborative Innovation Center of Advanced Microstructures, and Jiangsu Physical Science Research Center, Nanjing University, Nanjing 210093, China;* orcid.org/0000-0002-3823-1272; Email: muwang@nju.edu.cn

Authors

Yi Zhu − *National Laboratory of Solid State Microstructures, School of Physics, Collaborative Innovation Center of Advanced Microstructures, and Jiangsu Physical Science Research Center, Nanjing University, Nanjing 210093, China*

Yu-Heng Hou − *National Laboratory of Solid State Microstructures, School of Physics, Collaborative Innovation Center of Advanced Microstructures, and Jiangsu Physical Science Research Center, Nanjing University, Nanjing 210093, China*

Qing Cai − *National Laboratory of Solid State Microstructures, School of Physics, Collaborative Innovation Center of Advanced Microstructures, and Jiangsu Physical Science Research Center, Nanjing University, Nanjing 210093, China*

Li-Jiong Chen − *National Laboratory of Solid State Microstructures, School of Physics, Collaborative Innovation Center of Advanced Microstructures, and Jiangsu Physical Science Research Center, Nanjing University, Nanjing 210093, China*

Complete contact information is available at: https://pubs.acs.org/10.1021/acs.nanolett.6c00536

Author Contributions

#Y.Z. and Y.H.H. contributed equally to this work. R.P., Y.Z, and M.W. conceived this work. Y.Z. fabricated the device with the assistance of Q.C. and L.J.C. Y.Z. and Y.H.H. performed the optical experiments and simulations. R.P. and M.W. directed the experiments and simulations. Y.Z., Y.H.H., R.P., and M.W. wrote the manuscript.

Notes

The authors declare no competing financial interest.

■ ACKNOWLEDGMENTS

The work was supported by the National Key R&D Program of China (Grant No. 2022YFA1404303), the National Natural Science Foundation of China (Grant No. 12234010), and the Natural Science Foundation of Jiangsu Province (No. BK20233001).

■ REFERENCES

(1) Yu, Z.; Fan, S. Complete optical isolation created by indirect interband photonic transitions. *Nat. Photonics* **2009**, *3* (2), 91−94.

(2) Sounas, D. L.; Alù, A. Non-reciprocal photonics based on time modulation. *Nat. Photonics* **2017**, *11* (12), 774−783.

(3) Asadchy, V. S.; Mirmoosa, M. S.; Díaz-Rubio, A.; Fan, S.; Tretyakov, S. A. Tutorial on Electromagnetic Nonreciprocity and its Origins. *Proc. IEEE* **2020**, *108* (10), 1684−1727.

(4) Tang, L.; Tang, J. s.; Xia, K. Chiral Quantum Optics and Optical Nonreciprocity Based on Susceptibility-Momentum Locking. *Advanced Quantum Technologies* **2022**, DOI: 10.1002/qute.202200014.

(5) Wang, Z. B.; Zhang, Y. L.; Hu, X. X.; Chen, G. J.; Li, M.; Yang, P. F.; Zou, X. B.; Zhang, P. F.; Dong, C. H.; Li, G.; Zhang, T. C.; Guo, G. C.; Zou, C. L. Self-induced optical non-reciprocity. *Light Sci. Appl.* **2025**, *14* (1), 23.

(6) Silveirinha, M. G. Hidden time-reversal symmetry in dissipative reciprocal systems. *Opt. Express* **2019**, *27* (10), 14328−14337.

(7) Zheng, A.; Zhang, G.; Chen, H.; Mei, T.; Liu, J. Nonreciprocal light propagation in coupled microcavities system beyond weak-excitation approximation. *Sci. Rep.* **2017**, *7* (1), 14001.

(8) Tripathi, A.; Ugwu, C. F.; Asadchy, V. S.; Faniayeu, I.; Kravchenko, I.; Fan, S.; Kivshar, Y.; Valentine, J.; Kruk, S. S. Nanoscale optical nonreciprocity with nonlinear metasurfaces. *Nat. Commun.* **2024**, *15* (1), 5077.

(9) Yang, W.; Qin, J.; Long, J.; Yan, W.; Yang, Y.; Li, C.; Li, E.; Hu, J.; Deng, L.; Du, Q.; Bi, L. A self-biased non-reciprocal magnetic metasurface for bidirectional phase modulation. *Nature Electronics* **2023**, *6* (3), 225−234.

(10) Ferreira, A.; Viana-Gomes, J.; Bludov, Y. V.; Pereira, V.; Peres, N. M. R.; Castro Neto, A. H. Faraday effect in graphene enclosed in an optical cavity and the equation of motion method for the study of magneto-optical transport in solids. *Phys. Rev. B* **2011**, *84* (23), 235410.

(11) Sun, Z.; Yi, Y.; Song, T.; Clark, G.; Huang, B.; Shan, Y.; Wu, S.; Huang, D.; Gao, C.; Chen, Z.; McGuire, M.; Cao, T.; Xiao, D.; Liu, W.-T.; Yao, W.; Xu, X.; Wu, S. Giant nonreciprocal second-harmonic generation from antiferromagnetic bilayer CrI(3). *Nature* **2019**, *572* (7770), 497−501.

(12) Toyoda, S.; Fiebig, M.; Arima, T. H.; Tokura, Y.; Ogawa, N. Nonreciprocal second harmonic generation in a magnetoelectric material. *Sci. Adv.* **2021**, DOI: 10.1126/sciadv.abe2793.

(13) Xu, Q.; Schmidt, B.; Pradhan, S.; Lipson, M. Micrometre-scale silicon electro-optic modulator. *Nature* **2005**, *435* (7040), 325−327.

(14) Phare, C. T.; Daniel Lee, Y.-H.; Cardenas, J.; Lipson, M. Graphene electro-optic modulator with 30 GHz bandwidth. *Nat. Photonics* **2015**, *9* (8), 511−514.

(15) Fan, Y.; Han, J.; Wei, Z.; Wu, C.; Cao, Y.; Yu, X.; Li, H. Subwavelength electromagnetic diode: One-way response of cascading nonlinear meta-atoms. *Appl. Phys. Lett.* **2011**, *98* (15), 151903.

(16) Mahmoud, A. M.; Davoyan, A. R.; Engheta, N. All-passive nonreciprocal metastructure. *Nat. Commun.* **2015**, *6* (1), 8359.
(17) Poutrina, E.; Urbas, A. Nonreciprocal on the Nanoscale: Nonlinear Generation via Multipole Interference. In *Nonlinear Optics*; Optica Publishing Group: Waikoloa, HI, 2017; p NM3B.5. DOI: 10.1364/NLO.2017.NM3B.5.
(18) Liu, M.; Xia, S.; Wan, W.; Qin, J.; Li, H.; Zhao, C.; Bi, L.; Qiu, C.-W. Broadband mid-infrared non-reciprocal absorption using magnetized gradient epsilon-near-zero thin films. *Nat. Mater.* **2023**, *22* (10), 1196−1202.
(19) Tsurimaki, Y.; Qian, X.; Pajovic, S.; Han, F.; Li, M.; Chen, G. J. Large nonreciprocal absorption and emission of radiation in type-I Weyl semimetals with time reversal symmetry breaking. *Phys. Rev. B* **2020**, DOI: 10.1103/PhysRevB.101.165426.
(20) Shayegan, K. J.; Zhao, B.; Kim, Y.; Fan, S.; Atwater, H. A. Nonreciprocal infrared absorption via resonant magneto-optical coupling to InAs. *Sci. Adv.* **2022**, *8* (18), No. eabm4308.
(21) Albano, G.; Lissia, M.; Pescitelli, G.; Aronica, L. A.; Di Bari, L. Chiroptical response inversion upon sample flipping in thin films of a chiral benzo[1,2-b:4,5-b′]dithiophene-based oligothiophene. *Materials Chemistry Frontiers* **2017**, *1* (10), 2047−2056.
(22) Albano, G.; Salerno, F.; Portus, L.; Porzio, W.; Aronica, L. A.; Di Bari, L. Outstanding Chiroptical Features of Thin Films of Chiral Oligothiophenes. *ChemNanoMat* **2018**, *4* (10), 1059−1070.
(23) von Weber, A.; Hooper, D. C.; Jakob, M.; Valev, V. K.; Kartouzian, A.; Heiz, U. Circular Dichroism and Isotropy - Polarity Reversal of Ellipticity in Molecular Films of 1,1'-Bi-2-Naphtol. *ChemPhysChem* **2019**, *20* (1), 62−69.
(24) Albano, G.; Górecki, M.; Pescitelli, G.; Di Bari, L.; Jávorfi, T.; Hussain, R.; Siligardi, G. Electronic circular dichroism imaging (CDi) maps local aggregation modes in thin films of chiral oligothiophenes. *New J. Chem.* **2019**, *43* (36), 14584−14593.
(25) Zinna, F.; Albano, G.; Taddeucci, A.; Colli, T.; Aronica, L. A.; Pescitelli, G.; Di Bari, L. Emergent Nonreciprocal Circularly Polarized Emission from an Organic Thin Film. *Adv. Mater.* **2020**, *32* (37), No. e2002575.
(26) Lin, L.-Z.; Huang, L.-Q.; You, S.-W.; Huang, Y.-J.; Zinna, F.; Salij, A.; Di Bari, L.; Goldsmith, R. H.; Tempelaar, R.; Huang, C.-Y.; Chen, T.-L. Circularly Polarized Stimulated Emission from a Chiral Cavity Based on Apparent Circular Dichroism Organic Thin Films. *ACS Photonics* **2025**, *12* (5), 2557−2565.
(27) Mak, K. F.; Lee, C.; Hone, J.; Shan, J.; Heinz, T. F. Atomically thin MoS(2): a new direct-gap semiconductor. *Phys. Rev. Lett.* **2010**, *105* (13), 136805.
(28) Splendiani, A.; Sun, L.; Zhang, Y.; Li, T.; Kim, J.; Chim, C.-Y.; Galli, G.; Wang, F. Emerging Photoluminescence in Monolayer MoS2. *Nano Lett.* **2010**, *10* (4), 1271−1275.
(29) Wang, G.; Chernikov, A.; Glazov, M. M.; Heinz, T. F.; Marie, X.; Amand, T.; Urbaszek, B. Colloquium: Excitons in atomically thin transition metal dichalcogenides. *Rev. Mod. Phys.* **2018**, *90* (2), 021001.
(30) Shi, J.; Yu, P.; Liu, F.; He, P.; Wang, R.; Qin, L.; Zhou, J.; Li, X.; Zhou, J.; Sui, X.; Zhang, S.; Zhang, Y.; Zhang, Q.; Sum, T. C.; Qiu, X.; Liu, Z.; Liu, X. 3R MoS2 with Broken Inversion Symmetry: A Promising Ultrathin Nonlinear Optical Device. *Adv. Mater.* **2017**, DOI: 10.1002/adma.201701486.
(31) Zhou, X.; Cheng, J.; Zhou, Y.; Cao, T.; Hong, H.; Liao, Z.; Wu, S.; Peng, H.; Liu, K.; Yu, D. Strong Second-Harmonic Generation in Atomic Layered GaSe. *J. Am. Chem. Soc.* **2015**, *137* (25), 7994−7997.
(32) Zograf, G.; Küçüköz, B.; Polyakov, A. Y.; Yankovich, A. B.; Ranjan, A.; Bancerek, M.; Agrawal, A. V.; Olsson, E.; Wieczorek, W.; Antosiewicz, T. J.; Shegai, T. O. Ultrathin 3R-MoS2 metasurfaces with atomically precise edges for efficient nonlinear nanophotonics. *Communications Physics* **2025**, DOI: 10.1038/s42005-025-02194-y.
(33) Huang, W.; Xiao, Y.; Xia, F.; Chen, X.; Zhai, T. Second Harmonic Generation Control in 2D Layered Materials: Status and Outlook. *Adv. Funct. Mater.* **2024**, *34* (16), 2310726.
(34) Zeng, Z.; Sun, X.; Zhang, D.; Zheng, W.; Fan, X.; He, M.; Xu, T.; Sun, L.; Wang, X.; Pan, A. Controlled Vapor Growth and Nonlinear Optical Applications of Large-Area 3R Phase WS2 and WSe2 Atomic Layers. *Adv. Funct. Mater.* **2019**, DOI: 10.1002/adfm.201806874.
(35) Du, L.; Tang, J.; Liang, J.; Liao, M.; Jia, Z.; Zhang, Q.; Zhao, Y.; Yang, R.; Shi, D.; Gu, L.; Xiang, J.; Liu, K.; Sun, Z.; Zhang, G. Giant Valley Coherence at Room Temperature in 3R WS(2) with Broken Inversion Symmetry. *Research* **2019**, *2019*, 6494565.
(36) Tang, Y.; Sripathy, K.; Qin, H.; Lu, Z.; Guccione, G.; Janousek, J.; Zhu, Y.; Hasan, M. M.; Iwasa, Y.; Lam, P. K.; Lu, Y. Quasi-phase-matching enabled by van der Waals stacking. *Nat. Commun.* **2024**, *15* (1), 9979.
(37) Trovatello, C.; Ferrante, C.; Yang, B.; Bajo, J.; Braun, B.; Peng, Z. H.; Xu, X.; Jenke, P. K.; Ye, A.; Delor, M.; Basov, D. N.; Park, J.; Walther, P.; Dean, C. R.; Rozema, L. A.; Marini, A.; Cerullo, G.; Schuck, P. J. Quasi-phase-matched up- and down-conversion in periodically poled layered semiconductors. *Nat. Photonics* **2025**, *19* (3), 291−299.
(38) Jiang, H.; Zheng, L.; Wang, J.; Xu, M.; Gan, X.; Wang, X.; Huang, W. Inversion symmetry broken in 2H phase vanadium-doped molybdenum disulfide. *Nanoscale* **2021**, *13* (43), 18103−18111.
(39) Mennel, L.; Furchi, M. M.; Wachter, S.; Paur, M.; Polyushkin, D. K.; Mueller, T. Optical imaging of strain in two-dimensional crystals. *Nat. Commun.* **2018**, *9* (1), 516.
(40) Wang, J.; Han, N.; Luo, Z.-D.; Zhang, M.; Chen, X.; Liu, Y.; Hao, Y.; Zhao, J.; Gan, X. Electrically Tunable Second Harmonic Generation in Atomically Thin ReS(2). *ACS Nano* **2022**, *16* (4), 6404−6413.
(41) Ren, M.; Plum, E.; Xu, J.; Zheludev, N. I. Giant nonlinear optical activity in a plasmonic metamaterial. *Nat. Commun.* **2012**, *3*, 833.
(42) Li, G.; Chen, S.; Pholchai, N.; Reineke, B.; Wong, P. W.; Pun, E. Y.; Cheah, K. W.; Zentgraf, T.; Zhang, S. Continuous control of the nonlinearity phase for harmonic generations. *Nat. Mater.* **2015**, *14* (6), 607−612.
(43) Li, G.; Zhang, S.; Zentgraf, T. Nonlinear photonic metasurfaces. *Nature Reviews Materials* **2017**, DOI: 10.1038/natrevmats.2017.10.
(44) Gao, Y.-J.; Xiong, X.; Wang, Z.; Chen, F.; Peng, R.-W.; Wang, M. Simultaneous Generation of Arbitrary Assembly of Polarization States with Geometrical-Scaling-Induced Phase Modulation. *Physical Review X* **2020**, DOI: 10.1103/PhysRevX.10.031035.
(45) Ma, J.; Xie, F.; Chen, W.; Chen, J.; Wu, W.; Liu, W.; Chen, Y.; Cai, W.; Ren, M.; Xu, J. Nonlinear Lithium Niobate Metasurfaces for Second Harmonic Generation. *Laser & Photonics Reviews* **2021**, DOI: 10.1002/lpor.202000521.
(46) Xiong, B.; Liu, Y.; Xu, Y.; Deng, L.; Chen, C. W.; Wang, J. N.; Peng, R.; Lai, Y.; Liu, Y.; Wang, M. Breaking the limitation of polarization multiplexing in optical metasurfaces with engineered noise. *Science* **2023**, *379* (6629), 294−299.
(47) Deng, J.; Hu, Z.; Chen, Y.; Chen, J.; Wang, H.; Li, K.; Kivshar, Y.; Li, G. Nonlinear Optical Information Encoding with Grayscale Lithography Enabled Metasurfaces. *Nano Lett.* **2025**, *25* (18), 7450−7456.
(48) Wang, Z.; Dong, Z.; Zhu, H.; Jin, L.; Chiu, M.-H.; Li, L.-J.; Xu, Q.-H.; Eda, G.; Maier, S. A.; Wee, A. T. S.; Qiu, C.-W.; Yang, J. K. W. Selectively Plasmon-Enhanced Second-Harmonic Generation from Monolayer Tungsten Diselenide on Flexible Substrates. *ACS Nano* **2018**, *12* (2), 1859−1867.
(49) Chen, J.; Wang, K.; Long, H.; Han, X.; Hu, H.; Liu, W.; Wang, B.; Lu, P. Tungsten Disulfide-Gold Nanohole Hybrid Metasurfaces for Nonlinear Metalenses in the Visible Region. *Nano Lett.* **2018**, *18* (2), 1344−1350.
(50) Hu, G.; Hong, X.; Wang, K.; Wu, J.; Xu, H.-X.; Zhao, W.; Liu, W.; Zhang, S.; Garcia-Vidal, F.; Wang, B.; Lu, P.; Qiu, C.-W. Coherent steering of nonlinear chiral valley photons with a synthetic Au-WS2 metasurface. *Nat. Photonics* **2019**, *13* (7), 467−472.
(51) Spreyer, F.; Zhao, R.; Huang, L.; Zentgraf, T. Second harmonic imaging of plasmonic Pancharatnam-Berry phase metasurfaces coupled to monolayers of WS2. *Nanophotonics* **2020**, *9* (2), 351−360.

https://doi.org/10.1021/acs.nanolett.6c00536
Nano Lett. XXXX, XXX, XXX−XXX

(52) Leng, Q.; Su, H.; Liu, J.; Zhou, L.; Qin, K.; Wang, Q.; Fu, J.; Wu, S.; Zhang, X. Enhanced second-harmonic generation in monolayer MoS2 on suspended metallic nanostructures by plasmonic resonances. *Nanophotonics* **2021**, *10* (7), 1871−1877.
(53) Bernhardt, N.; Koshelev, K.; White, S. J. U.; Meng, K. W. C.; Froch, J. E.; Kim, S.; Tran, T. T.; Choi, D.-Y.; Kivshar, Y.; Solntsev, A. S. Quasi-BIC Resonant Enhancement of Second-Harmonic Generation in WS(2) Monolayers. *Nano Lett.* **2020**, *20* (7), 5309−5314.
(54) Green, T. D.; Baranov, D. G.; Munkhbat, B.; Verre, R.; Shegai, T.; Käll, M. Optical material anisotropy in high-index transition metal dichalcogenide Mie nanoresonators. *Optica* **2020**, *7* (6), 680.
(55) Nauman, M.; Yan, J.; de Ceglia, D.; Rahmani, M.; Zangeneh Kamali, K.; De Angelis, C.; Miroshnichenko, A. E.; Lu, Y.; Neshev, D. N. Tunable unidirectional nonlinear emission from transition-metal-dichalcogenide metasurfaces. *Nat. Commun.* **2021**, *12* (1), 5597.
(56) Popkova, A. A.; Antropov, I. M.; Tselikov, G.; Ermolaev, G. A.; Ozerov, I.; Kirtaev, R.; Novikov, S. M.; Evlyukhin, A. B.; Arsenin, A.; Bessonov, V. O.; Volkov, V. S.; Fedyanin, A. A. Nonlinear Exciton-Mie Coupling in Transition Metal Dichalcogenide Nanoresonators. *Laser & Photonics Reviews* **2022**, DOI: 10.1002/lpor.202100604.
(57) Ling, H.; Tang, Y.; Tian, X.; Shafirin, P.; Hossain, M.; Vabishchevich, P. P.; Harutyunyan, H.; Davoyan, A. R. Nonlinear van der Waals Metasurfaces with Resonantly Enhanced Light Generation. *Nano Lett.* **2025**, *25* (23), 9229−9236.
(58) Tonkaev, P.; Toftul, I.; Lu, Z.; Qin, H.; Qiu, S.; Yang, W.; Koshelev, K.; Lu, Y.; Kivshar, Y. Nonlinear Chiral Metasurfaces Based on Structured van der Waals Materials. *Nano Lett.* **2024**, *24* (34), 10577−10582.
(59) Tang, J.; Gao, M.; Zhang, Q.; Yang, Y. Giant second-harmonic generation in rhombohedral transition metal dichalcogenide metasurfaces. *Opt. Commun.* **2025**, *584*, 131825.
(60) Fan, T.; Tang, Y.; Lung, S.; Weissflog, M.; Ma, J.; Shinde, S.; Saravi, S.; Nauman, M.; Yang, W.; Qin, H.; Qiu, S.; Sukhorukov, A. A.; Lu, Y.; Setzpfandt, F. Enhanced Photon-Pair Generation from a van der Waals Metasurface. *Nano Lett.* **2025**, *25* (31), 11844−11851.
(61) Peng, Z. H.; Cotrufo, M.; Xu, D.; Mann, S. A.; Qiu, S.; Basov, D. N.; Delor, M.; Alú, A.; Schuck, P. J.; Trovatello, C. 3R-stacked transition metal dichalcogenide non-local metasurface for efficient second-harmonic generation. *Nat. Photonics* **2025**, *19* (12), 1376−1384.
(62) Tang, Y.; Cohen, A. E. Optical chirality and its interaction with matter. *Phys. Rev. Lett.* **2010**, *104* (16), 163901.
(63) Spreyer, F.; Mun, J.; Kim, H.; Kim, R. M.; Nam, K. T.; Rho, J.; Zentgraf, T. Second Harmonic Optical Circular Dichroism of Plasmonic Chiral Helicoid-III Nanoparticles. *ACS Photonics* **2022**, *9* (3), 784−792.
(64) Jeong, M.; Lee, J.; Kim, S.; Gong, X.; Fang, R.; Yang, Y.; Chae, S. H.; Rho, J. Obtuse-angled separation of chiral resonances with planar asymmetry-induced tunability of quality factors. *Science advances* **2025**, *11* (30), No. eadu4875.
(65) Mun, J.; Kim, M.; Yang, Y.; Badloe, T.; Ni, J.; Chen, Y.; Qiu, C. W.; Rho, J. Electromagnetic chirality: from fundamentals to nontraditional chiroptical phenomena. *Light Sci. Appl.* **2020**, *9*, 139.
(66) He, J.; Li, C.-Y.; Qi, D.-X.; Cai, Q.; Liu, Y.; Fan, R.-H.; Su, J.; Huo, P.; Xu, T.; Peng, R.; Wang, M. Improving Photoelectric Conversion with Broadband Perovskite Metasurface. *Nano Lett.* **2022**, *22* (16), 6655−6663.
(67) Brongersma, M. L.; Cui, Y.; Fan, S. Light management for photovoltaics using high-index nanostructures. *Nat. Mater.* **2014**, *13* (5), 451−460.
(68) Seidt, L.; Weber, T.; Seredin, A. A.; Possmayer, T.; Savelev, R.; Petrov, M. I.; Maier, S. A.; Tittl, A.; Menezes, L. S.; Sortino, L. Ultrafast all-optical switching in nonlinear 3R-MoS(2) van der Waals metasurfaces. *Npj Nanophoton* **2025**, *2* (1), 37.
(69) Hong, H.; Huang, C.; Ma, C.; Qi, J.; Shi, X.; Liu, C.; Wu, S.; Sun, Z.; Wang, E.; Liu, K. Twist Phase Matching in Two-Dimensional Materials. *Phys. Rev. Lett.* **2023**, *131* (23), 233801.
(70) Tang, H.; Wang, Y.; Ni, X.; Watanabe, K.; Taniguchi, T.; Jarillo-Herrero, P.; Fan, S.; Mazur, E.; Yacoby, A.; Cao, Y. On-chip multi-degree-of-freedom control of two-dimensional materials. *Nature* **2024**, *632* (8027), 1038−1044.
(71) Zhou, H.; Ni, X.; Lou, B.; Fan, S.; Cao, Y.; Tang, H. Control of Chirality and Directionality of Nonlinear Metasurface Light Source via Moire Engineering. *Phys. Rev. Lett.* **2025**, *134* (4), 043801.
(72) Sun, J.; Hu, H.; Pan, D.; Zhang, S.; Xu, H. Selectively Depopulating Valley-Polarized Excitons in Monolayer MoS(2) by Local Chirality in Single Plasmonic Nanocavity. *Nano Lett.* **2020**, *20* (7), 4953−4959.
(73) Chen, Z.; Shen, F.; Zhang, Z.; Wu, K.; Jin, Y.; Long, M.; Wang, S.; Xu, J. Synergistic Effect of Chiral Metasurface and Hot Carrier Injection Enabling Manipulation of Valley Polarization of WSe2 at Room Temperature. *Advanced Physics Research* **2024**, DOI: 10.1002/apxr.202300062.
(74) Zhu, Y.; Zou, K. L.; Qi, D. X.; He, J.; Peng, R.; Wang, M. Tailoring Valley Polarization of Interlayer Excitons in van der Waals Heterostructure toward Optical Communication. *Nano Lett.* **2025**, *25* (21), 8680−8688.
(75) Ren, J.; Franke, S.; VanDrunen, B.; Hughes, S. Classical Purcell factors and spontaneous emission decay rates in a linear gain medium. *Phys. Rev. A* **2024**, DOI: 10.1103/PhysRevA.109.013513.
(76) Ding, F.; Pors, A.; Chen, Y.; Zenin, V. A.; Bozhevolnyi, S. I. Beam-Size-Invariant Spectropolarimeters Using Gap-Plasmon Metasurfaces. *ACS Photonics* **2017**, *4* (4), 943−949.
(77) Zheng, C.; Li, H.; Liu, J.; Wang, M.; Zang, H.; Zhang, Y.; Yao, J. Full-Stokes metasurface polarimetry requiring only a single measurement. *Photonics Research* **2024**, *12* (3), 514.
(78) Uribe Castaño, L.; Mirsanaye, K.; Kontenis, L.; Krouglov, S.; Žurauskas, E.; Navab, R.; Yasufuku, K.; Tsao, M.-S.; Akens, M. K.; Wilson, B. C.; Barzda, V. Wide-field Stokes polarimetric microscopy for second harmonic generation imaging. *Journal of Biophotonics* **2023**, DOI: 10.1002/jbio.202200284.
(79) Guo, Z.; Li, J.; Liang, J.; Wang, C.; Zhu, X.; He, T. Regulating Optical Activity and Anisotropic Second-Harmonic Generation in Zero-Dimensional Hybrid Copper Halides. *Nano Lett.* **2022**, *22* (2), 846−852.

https://doi.org/10.1021/acs.nanolett.6c00536
Nano Lett. XXXX, XXX, XXX−XXX